ADVANCED ENERGY MATERIALS

Supporting Information

for *Adv. Energy Mater.,* DOI: 10.1002/aenm.201802534

Synergistic Effect of 3D Current Collectors and ALD Surface Modification for High Coulombic Efficiency Lithium Metal Anodes

*Kuan-Hung Chen, Adrian J. Sanchez, Eric Kazyak, Andrew L. Davis, and Neil P. Dasgupta**

Supporting Information

Synergistic Effect of 3-D Current Collectors and ALD Surface Modification for High Coulombic Efficiency Lithium Metal Anodes

*Kuan-Hung Chen, Adrian J. Sanchez, Eric Kazyak, Andrew L. Davis, and Neil P. Dasgupta**

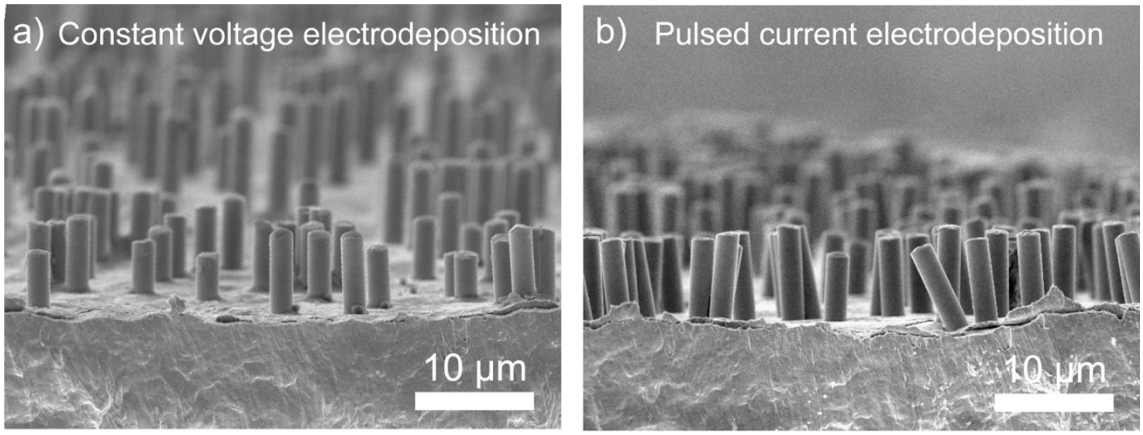

Figure S1. Cross-sectional SEM images of the 2 μm Cu pillars from (a) constant voltage electrodeposition and (b) pulsed current electrodeposition. Cu pillar arrays with uniform pillar length can be achieved using the pulsed electroplating method.

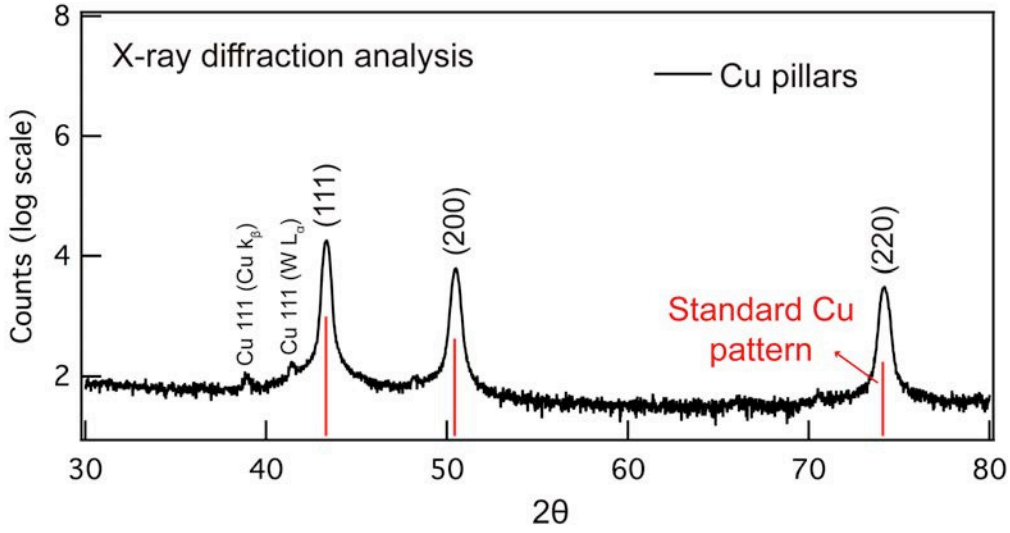

Figure S2. X-ray diffraction pattern of the electroplated Cu pillars showing crystalline Cu peaks. Major peaks are indexed and compared to ICDD PDF card 04-010-6011. Weak peaks are due to diffraction from Cu K_b and W L_α spectral contamination.

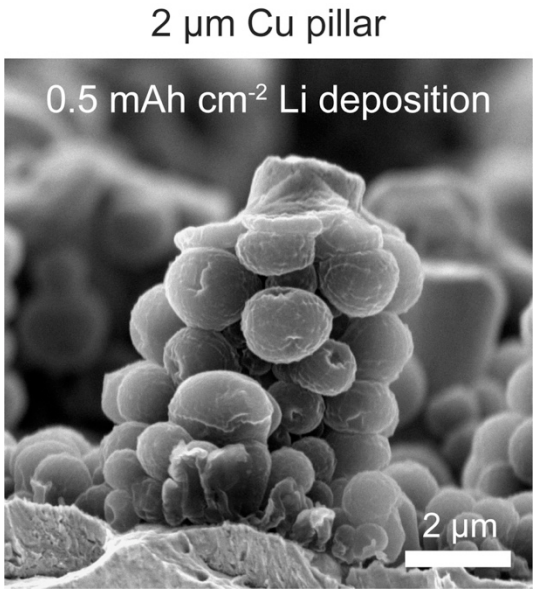

Figure S3. Cross-sectional SEM image of 2 μm Cu pillars upon 0.5 mAh/cm^2 of Li deposition (cross-sectional view of Figure 2g in the main text). The current density was fixed at 1 mA/cm^2. It was observed that Li deposits filled into the void space between Cu pillars and deposited conformally along the Cu pillars.

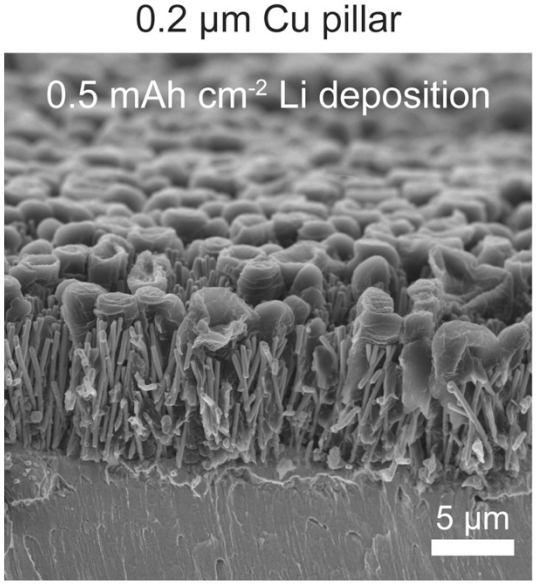

Figure S4. Cross-sectional SEM image of 0.2 μm Cu pillars upon 0.5 mAh/cm^2 of Li deposition (cross-sectional view of Figure 2d in the main text). The current density was fixed at 1 mA/cm^2. Li deposition was found to occur on top of the pillar arrays rather than within the 3-D Cu pillar structure.

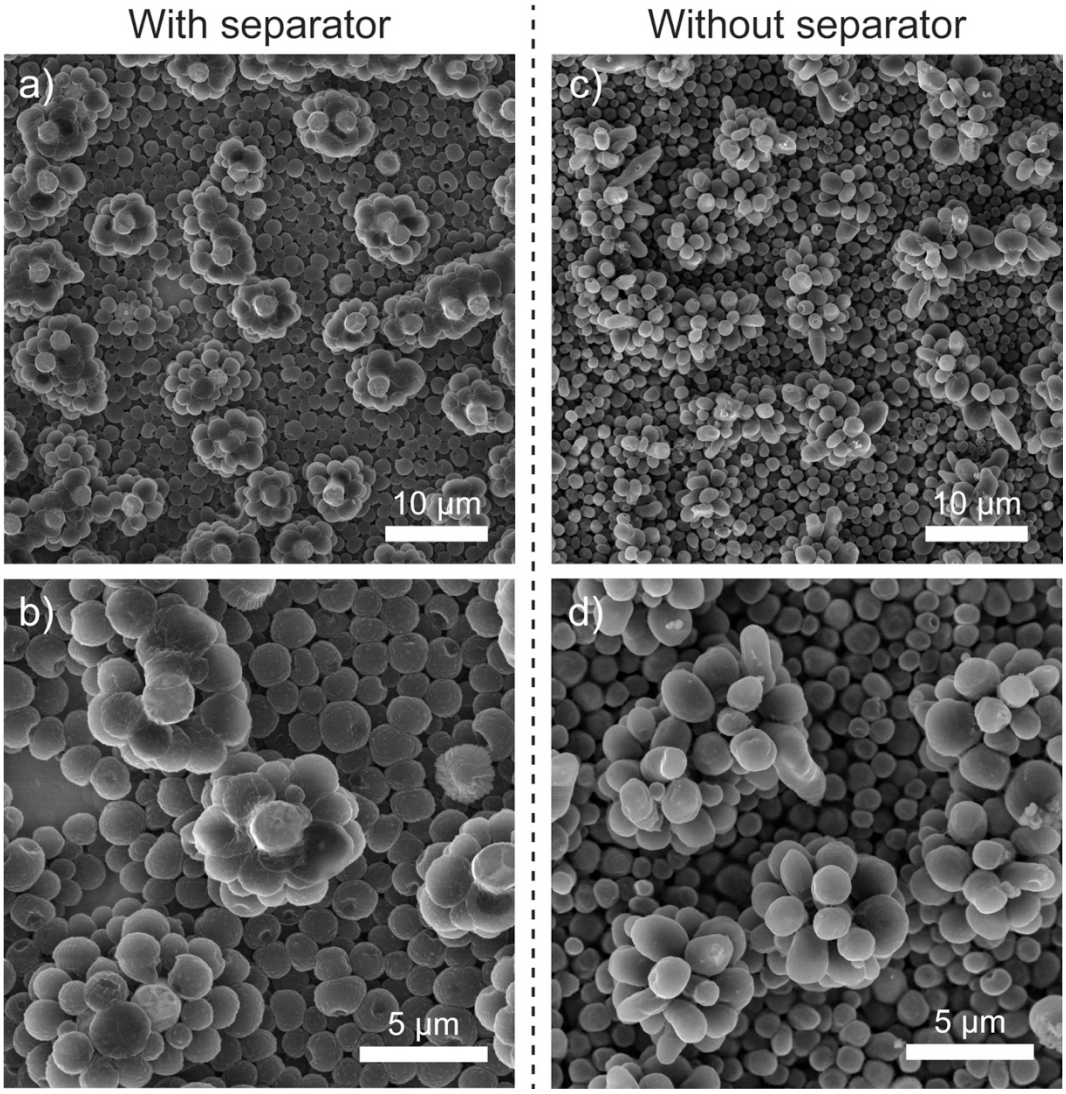

Figure S5. SEM morphology study of Li deposition on the 2 μm Cu pillars (a, b) with and (c, d) without the presence of the polymer separator. It was found that Li deposition occurred uniformly along the Cu pillar surface (including the tops of the pillars) in the cell assembled without a separator.

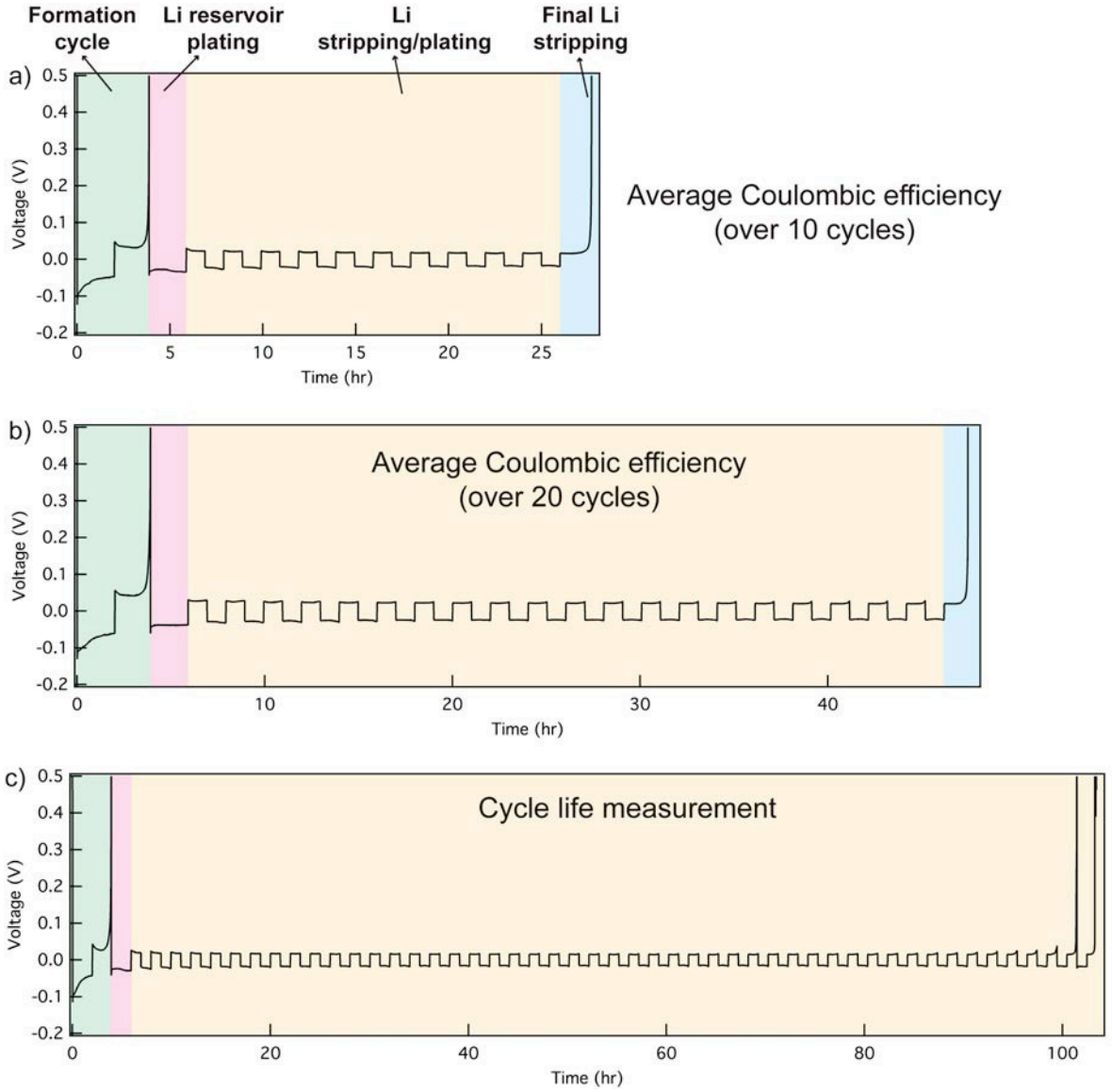

Figure S6. Voltage profiles of (a) average Coulombic efficiency measurement over 10 cycles, (b) average Coulombic efficiency measurement over 20 cycles, and (c) cycle life measurement. The formation cycle (green), Li reservoir plating (red), Li stripping/plating (yellow), and final Li stripping (blue) steps are highlighted in the figure. A fixed current density was applied throughout the cycling to ensure an accurate measurement.

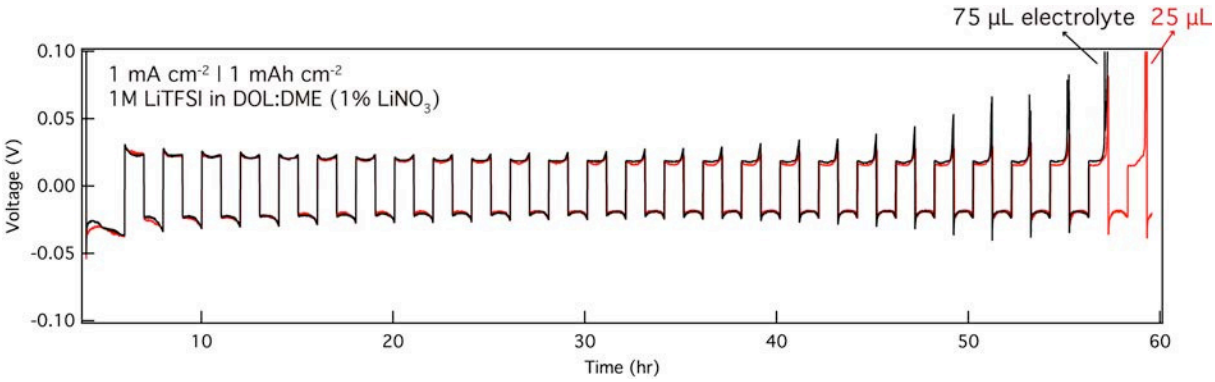

Figure S7. Galvanostatic cycling of Li-Cu cells with 75 µL (black) and 25 µL (red) of electrolyte showing that Li depletion on Cu electrode occurred sooner than the depletion of electrolyte. The failure mechanism is thus not convoluted by electrolyte drying-up.

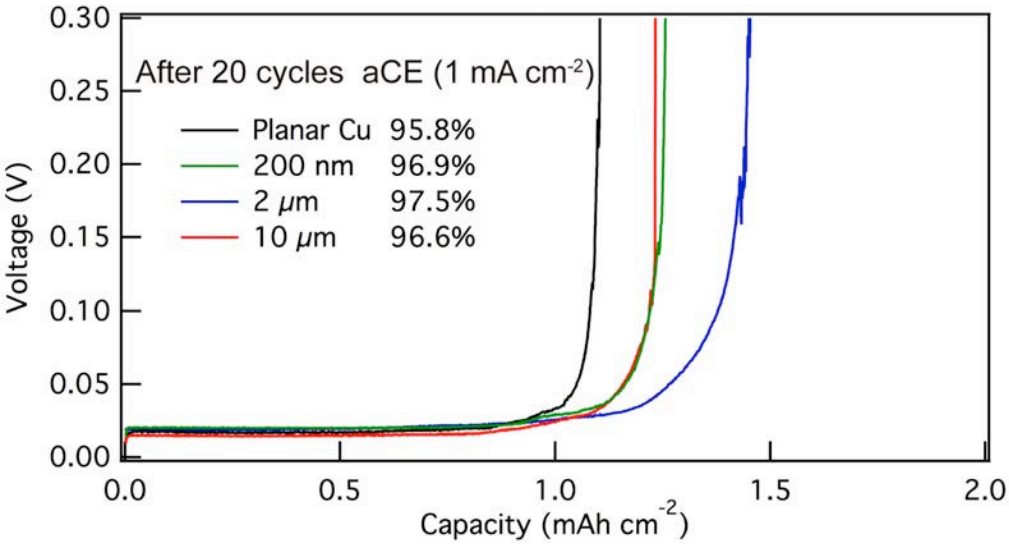

Figure S8. Average Coulombic efficiency measurements of pristine planar Cu, 0.2 µm pillars, 2 µm pillars, and 10 µm pillars over 20 cycles. The current density was 1 mA/cm^2.

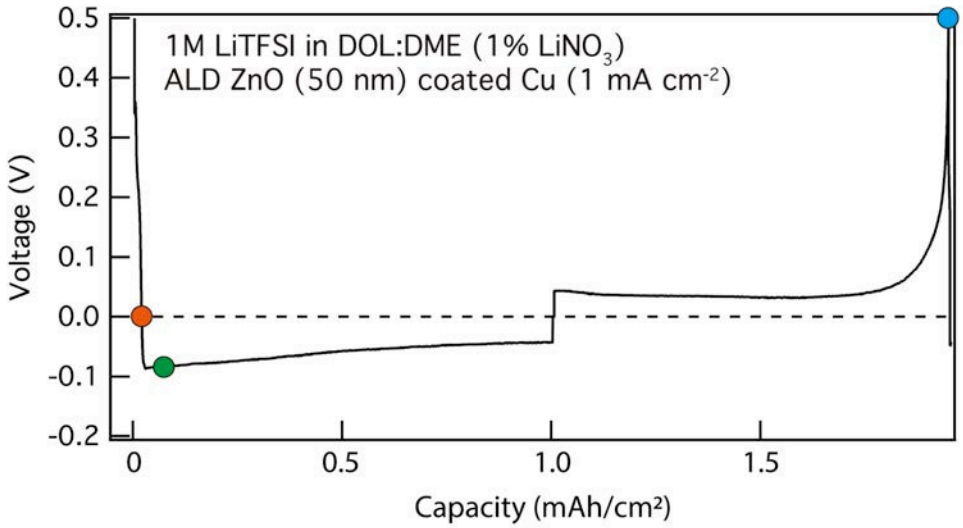

	Zn [%]	Li [%]	O [%]	C [%]
Lithiated to 0 V	3.4	55.4	34.4	3.6
Plated 0.1 mAh/cm² Li	0.0	58.7	26.7	3.7
Stripped to 0.5 V	1.3	54.8	32.7	5.7

10 min Ar sputter to remove adventitious film

Figure S9. XPS analysis of ALD ZnO coated planar Cu upon lithiation to 0 V (orange), 0.1 mAh/cm^2 of Li deposition (green), and Li stripping to 0.5 V (blue). Table of survey spectra quantification showing the presence of Zn upon lithiation to 0 V and after stripping, but no Zn signal was detected after 0.1 mAh/cm^2 of Li plating, suggesting Li plating occurred on top of the buffer layer.

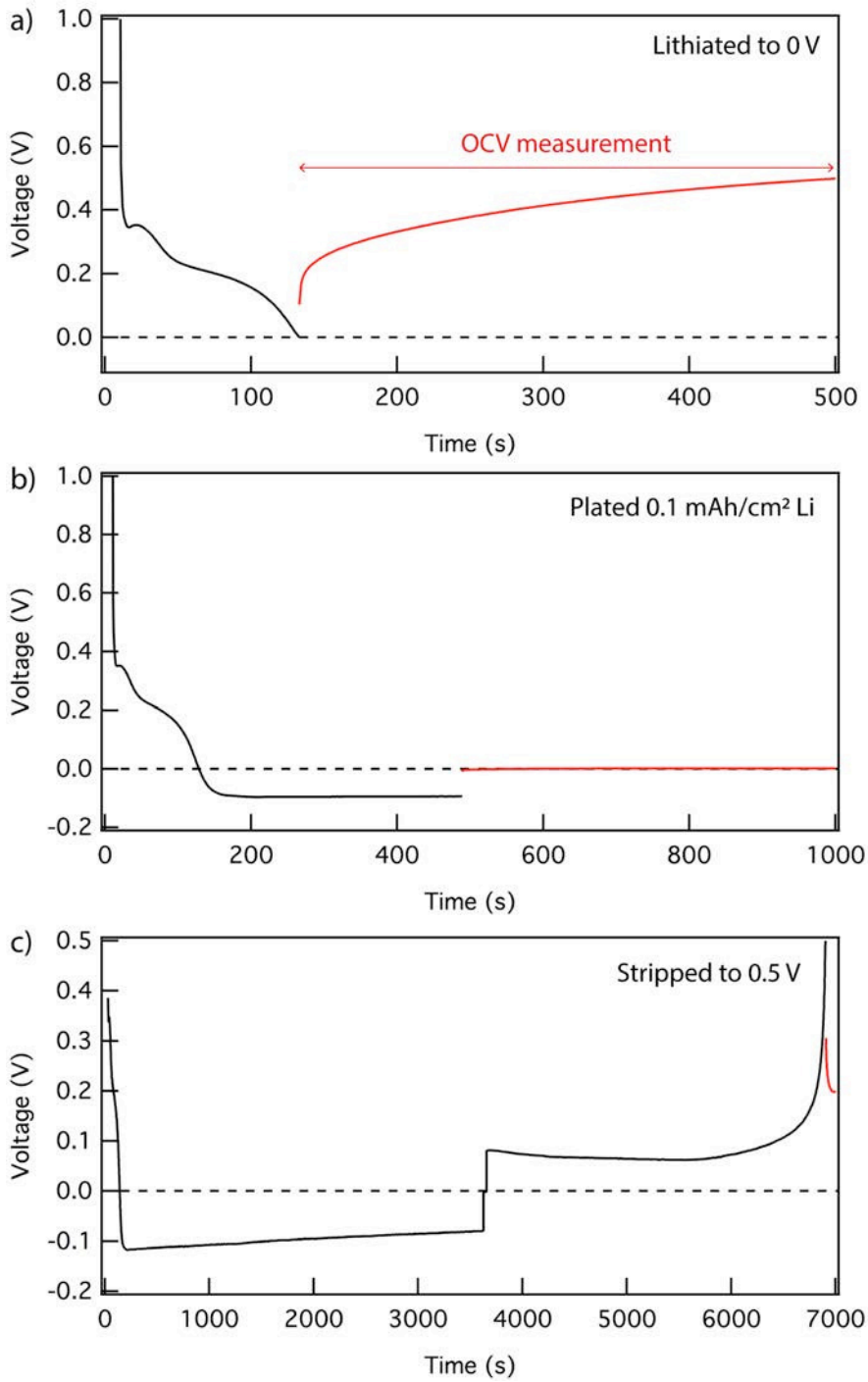

Figure S10. Open-circuit voltage (OCV) measurements upon (a) lithiation to 0 V, (b) 0.1 mAh/cm^2 of Li deposition, and (c) Li stripping to 0.5 V. It was found that after 0.1 mAh/cm^2 of Li plating the OCV stayed at 0 V (vs. Li/Li$^+$), indicating Li plating occurred on top of the buffer layer.

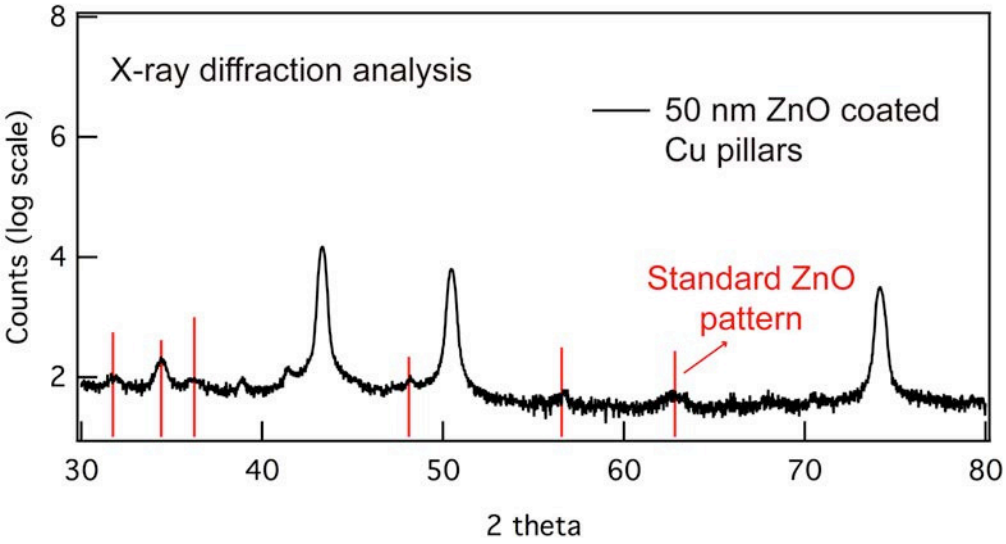

Figure S11. X-ray diffraction pattern of the ALD ZnO coated Cu pillars showing crystalline ZnO peaks. Peaks are indexed and compared to ICDD PDF card 04-016-6648.

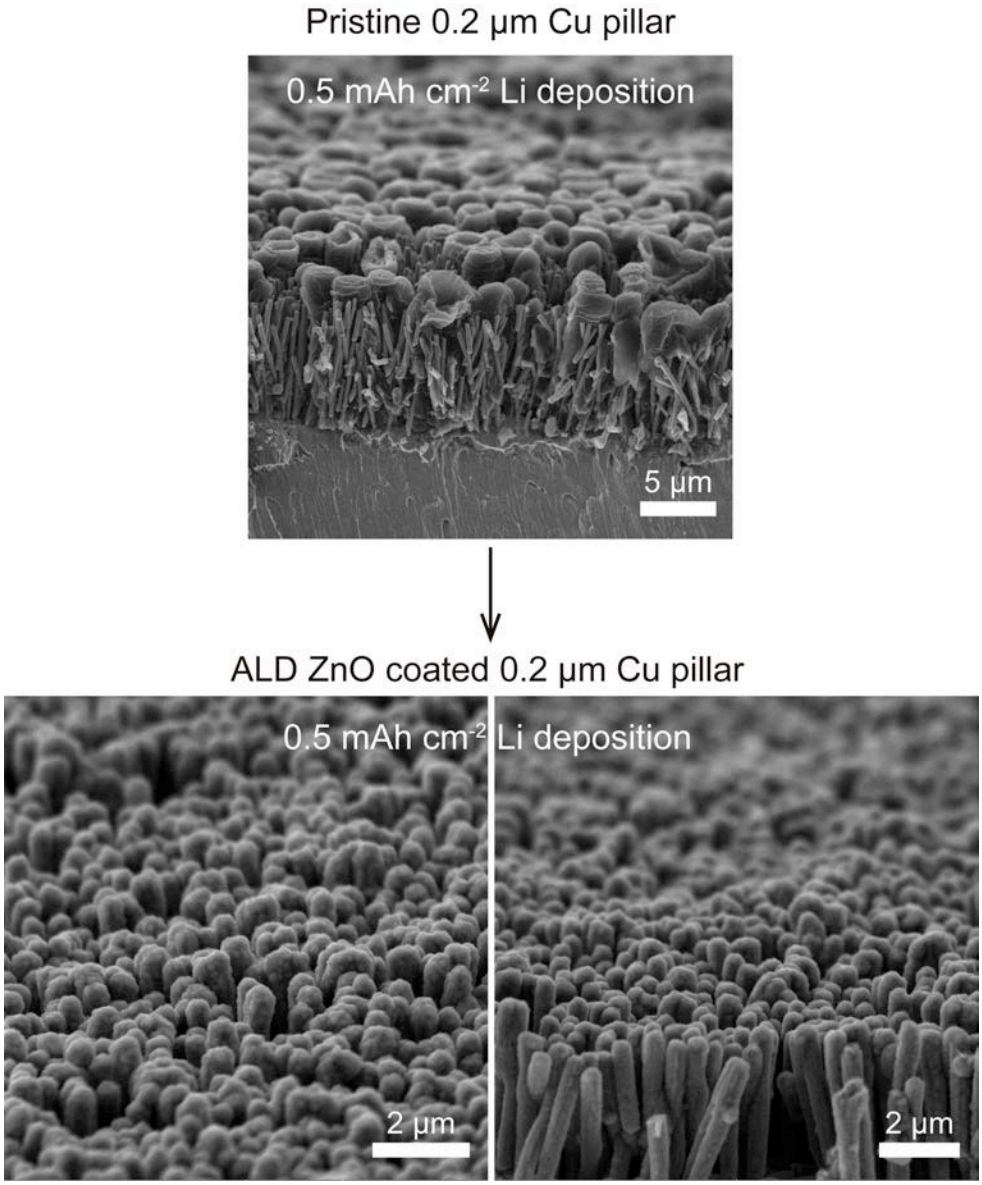

Figure S12. Cross-sectional SEM images of pristine and ALD ZnO coated 0.2 μm Cu pillars upon 0.5 mAh/cm^2 of Li deposition. The current density was fixed at 1 mA/cm^2. Li deposition was found to occur within the ZnO coated pillar arrays, suggesting the ALD coating can guide the Li plating into the 3-D structures.

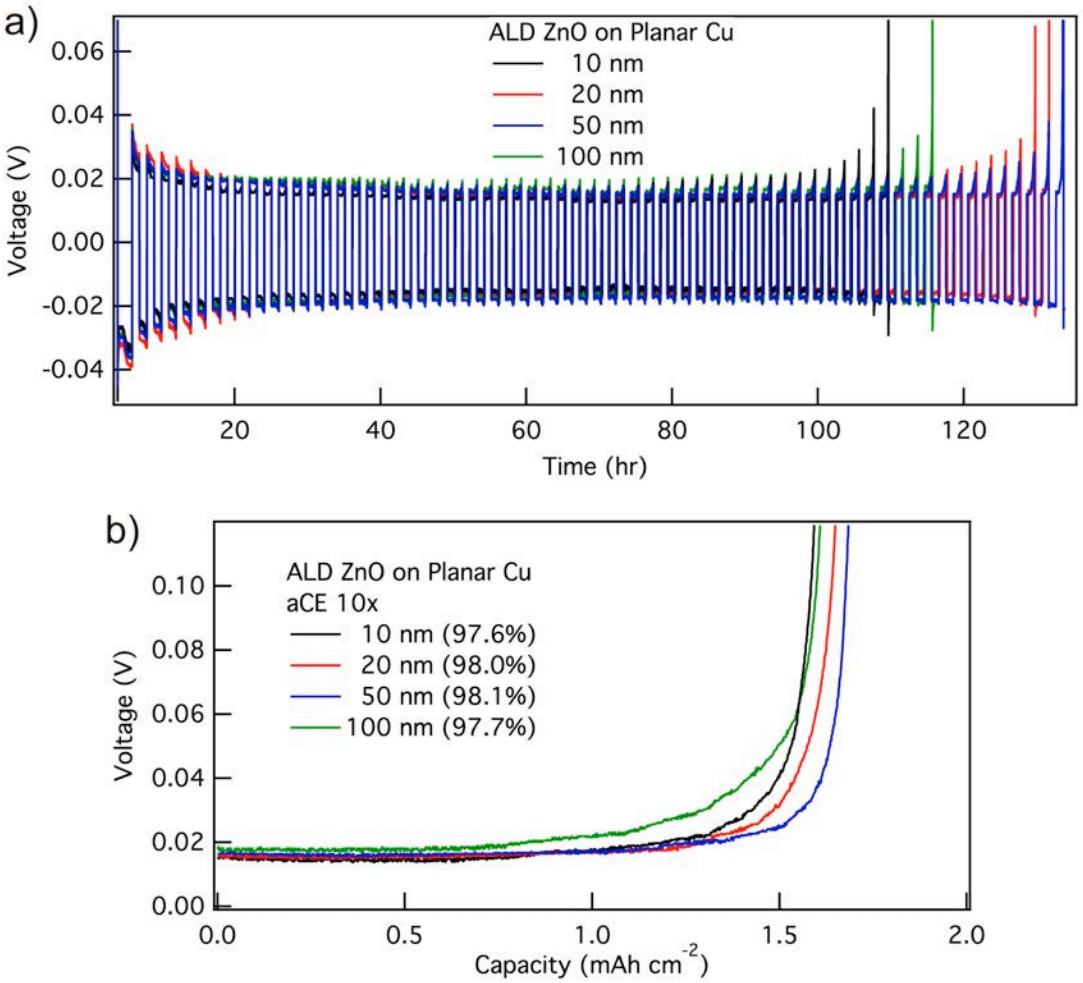

Figure S13. (a) Cycle life measurements of ALD coated planar Cu with 10 nm, 20 nm, 50 nm, and 100 nm of ZnO coating. (b) Corresponding average Coulombic efficiency measurements over 10 cycles. The current density was 1 mA/cm^2.

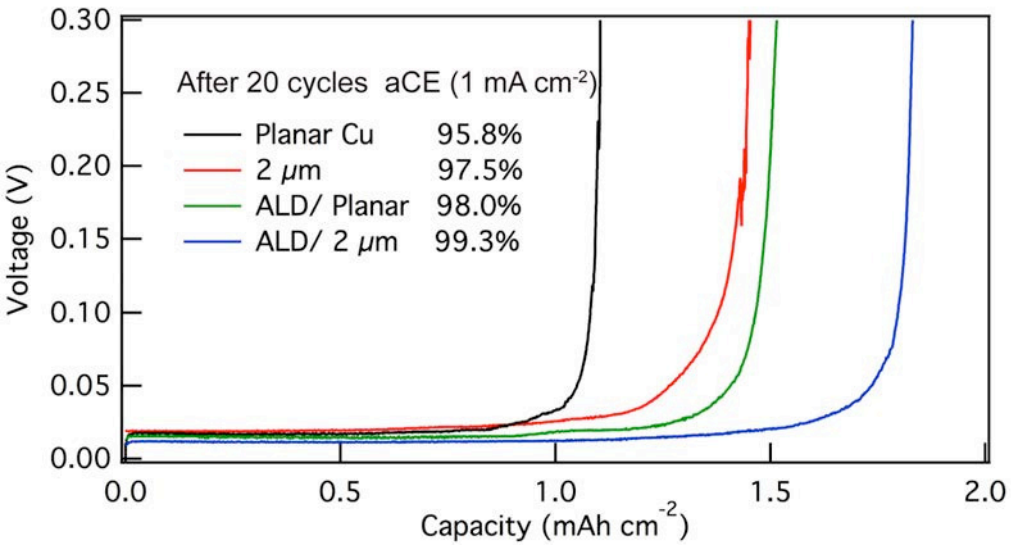

Figure S14. Average Coulombic efficiency measurements of planar Cu, 2 μm pillars, ALD coated planar Cu, and ALD coated 2 μm pillars over 20 cycles. The current density was 1 mA/cm^2.

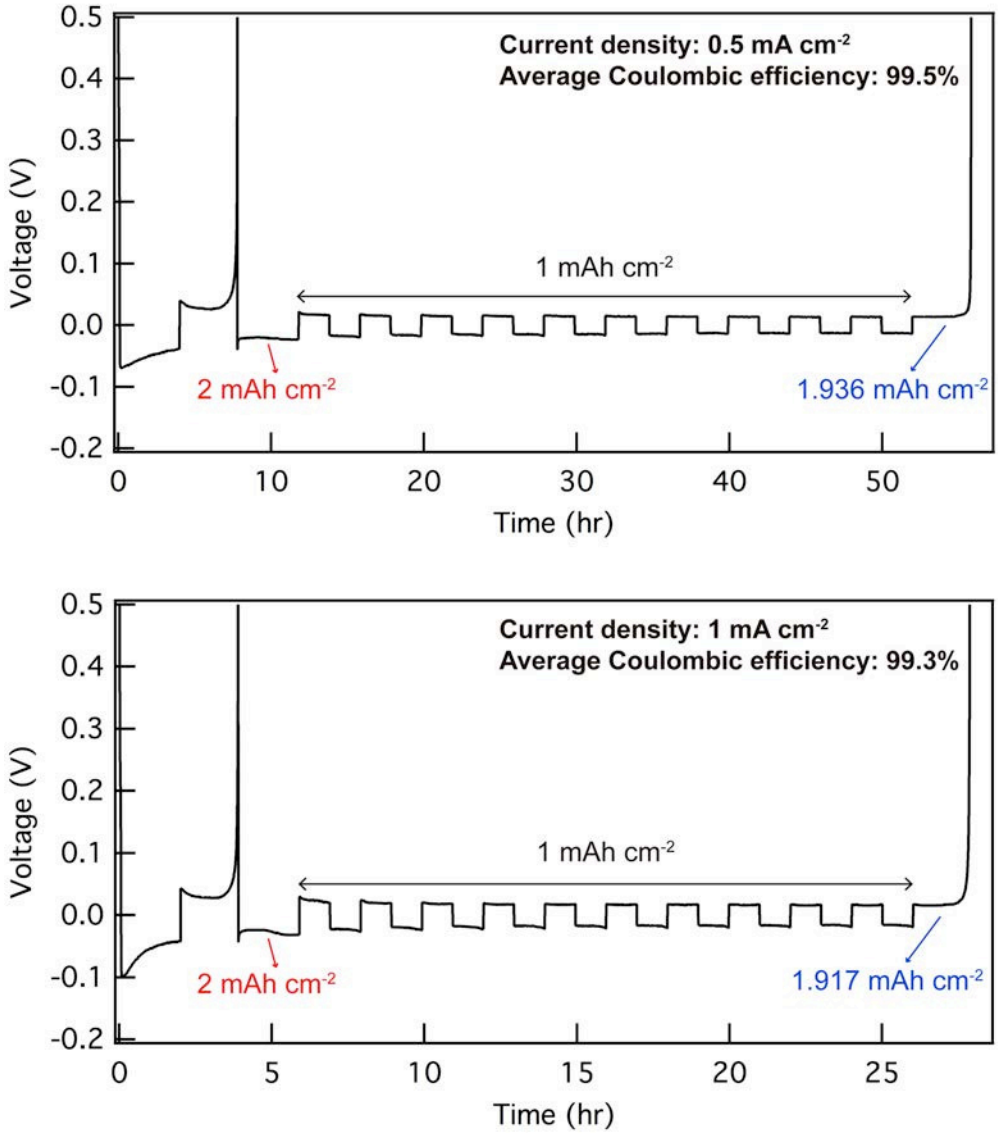

Figure S15. Detailed voltage profiles of the efficiency measurements of the ALD coated 2 μm pillars over 10 cycles. Coulombic efficiencies as high as 99.5 % and 99.3 % can be achieved under a current density of 0.5 mA/cm^2 and 1 mA/cm^2, respectively. The per-cycle areal capacity was fixed at 1 mAh/cm^2.

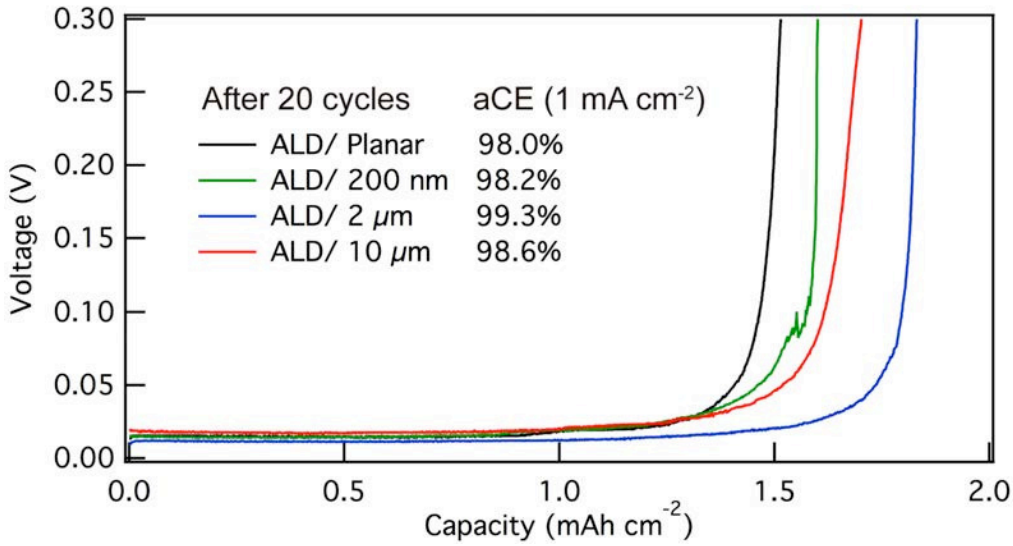

Figure S16. Average Coulombic efficiency measurements of ALD coated planar Cu, 0.2 μm pillars, 2 μm pillars, and 10 μm pillars over 20 cycles. The current density was 1 mA/cm^2.

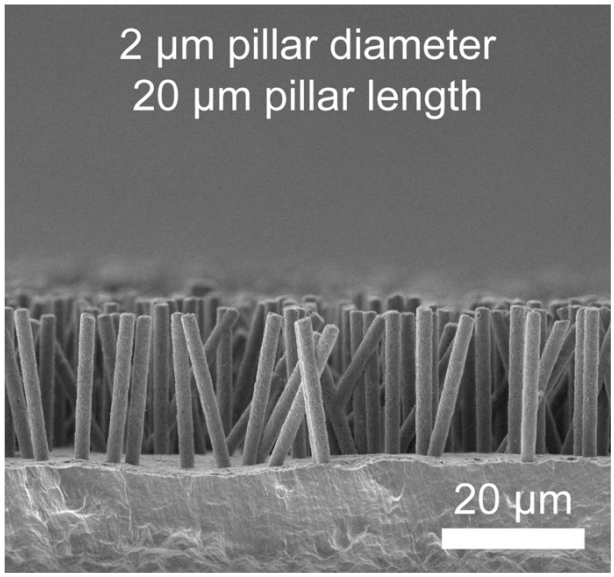

Figure S17. Cross-sectional SEM image of the 2 μm Cu pillars with 20 μm pillar length by pulsed current electrodeposition.

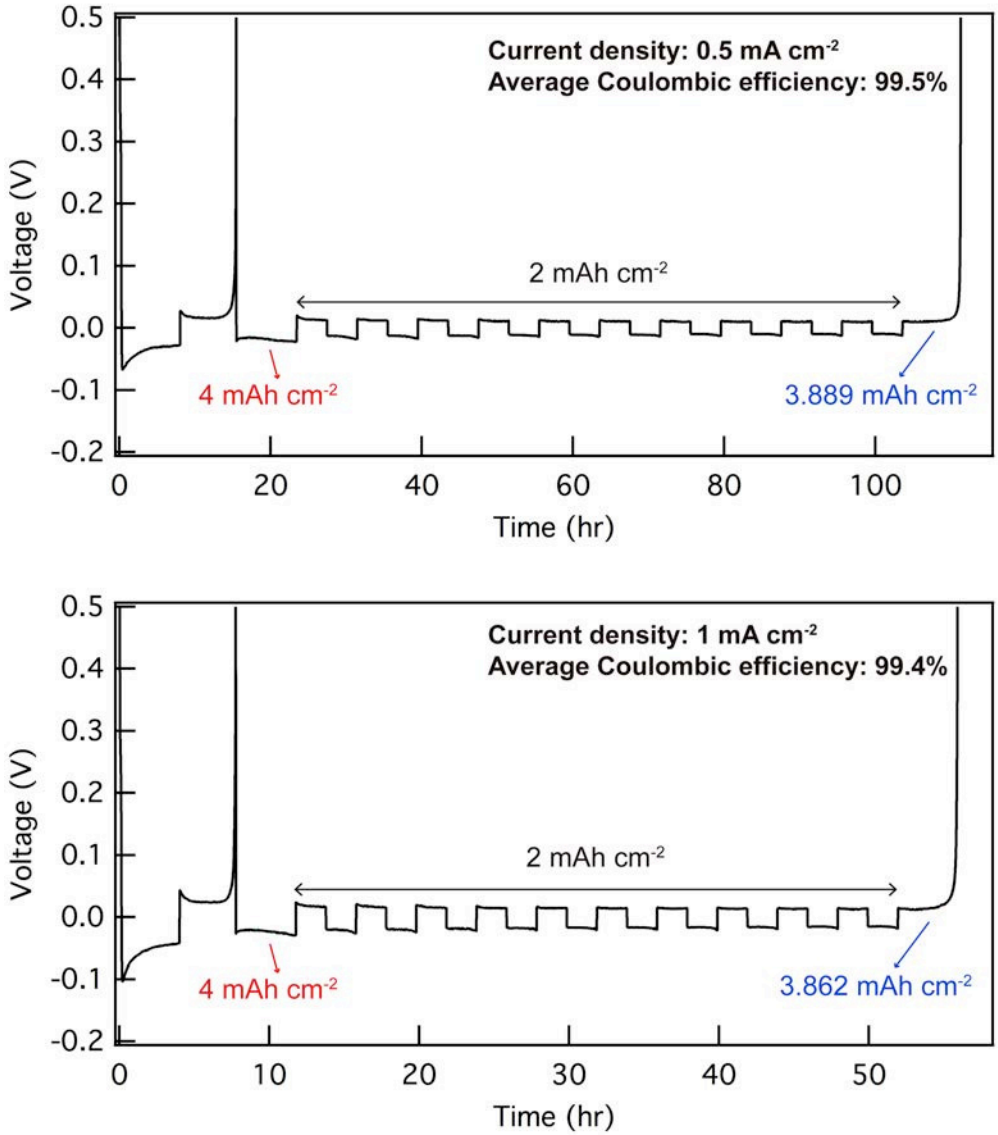

Figure S18. Detailed voltage profiles during the efficiency measurements of the ALD coated 2 μm pillars over 10 cycles. Coulombic efficiencies as high as 99.5 % and 99.4 % can be achieved under a current density of 0.5 mA/cm^2 and 1 mA/cm^2, respectively. The per-cycle areal capacity was fixed at 2 mAh/cm^2 and the pillar length was fixed at 20 μm.

Table S1.

Electrode treatment	Coulombic efficiency (%)	Current density (mA/cm^2)	Areal capacity (mAh/cm^2)	Electrolyte	Reference
Synergistic effect of 3-D current collectors and ALD surface modification	**99.5** **99.5** **99.4** **99.3** **99.4** **99.1**	0.5 0.5 1 1 2 2	2 1 2 1 2 1	DOL/DME (1% $LiNO_3$)	This work
Localized high-concentration electrolyte	**99.5** **99.4**	0.5 1	1 1	LiFSI/DMC-BTFE	Chen *et al.* 2018[1]
Double-layer nanodiamond interface	**99.4** **99.4** **99.2**	0.5 1 2	1 2 2	DOL/DME (2% $LiNO_3$)	Liu *et al.* 2018[2]
LiF ALD coatings	99.5 98.5	0.4 1	0.4 1	DOL/DME (2% $LiNO_3$ + 0.18M Li_2S_8)	Chen *et al.* 2018[3]
Vertically aligned microchannels	98.5	1	3	DOL/DME (1% $LiNO_3$)	Wang *et al.* 2017[4]
3-D TiC-C core-shell nanowire skeleton	98.5	1	1	DOL/DME (1% $LiNO_3$)	Liu *et al.* 2017[5]
Silver nanoparticles on carbon nanofibers	98.0	0.5	1	DOL/DME	Yang *et al.* 2017[6]
Cu_3N-polymer composite artificial SEI	98.3 97.6	0.5 1	1 1	DOL/DME (1% $LiNO_3$)	Liu *et al.* 2017[7]
Polyacrylonitrile submicron fiber array	98.1 97.4	0.5 1	1 1	DOL/DME (2% $LiNO_3$)	Lang *et al.* 2017[8]
Free-standing copper nanowire network	98.6	1	2	DOL/DME (1% $LiNO_3$ + 5mM Li_2S_8)	Lu *et al.* 2016[9]
Polyimide nanochannel confinement	97.6	1	0.5	DOL/DME (1% $LiNO_3$)	Liu *et al.* 2016[10]
Chemical dealloying derived 3-D porous current collector	97.0 97.0	0.5 1	1 1	DOL/DME (1% $LiNO_3$)	Yun *et al.* 2016[11]
3-D Cu submicron skeleton current collectors	98.5	0.5	1	DOL/DME (1% $LiNO_3$ + 5mM Li_2S_6)	Yang *et al.* 2015[12]

* DOL/DME represents 1M LiTFSI in DOL:DME (1:1)

* **Bold efficiency values** were measured using average Coulombic efficiency method proposed by Adams *et al.*[13] The others were measured by exhaustive Li stripping for each cycle (i.e. cycle-by-cycle efficiency).

Spacing Measurement Details:

Multiple SEM images of each pillar configuration were taken and analyzed to identify the average spacing between pillars. For a given SEM image, the surrounding area of a randomly chosen pillar was divided into quadrants as depicted in Figure S19. Each quadrant was searched for the nearest neighboring pillar (pillars circled in yellow). The distance (length of double headed arrow) to each of these nearest neighbors was averaged to estimate the spacing. This analysis was done on multiple SEM images to capture variations in spacing across the current collector. The results of this methodology are shown in Table S1. The average spacing was found to be roughly 2.5x greater than the diameter of the Cu pillars.

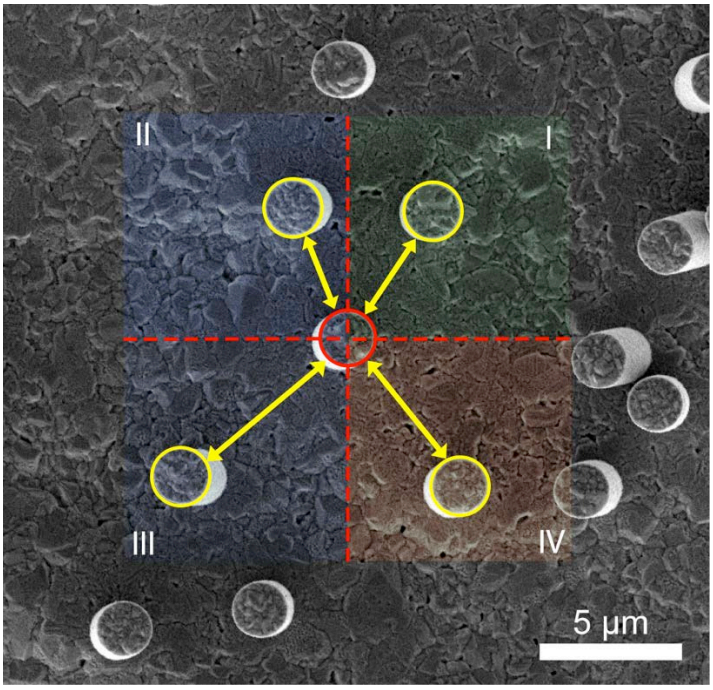

Figure S19. SEM image showing the nearest neighbors (yellow) of a chosen pillar (red) and their distances.

Pillar Diameter	Average Spacing (μm)	Standard Deviation (μm)
0.2 μm	0.49	0.19
2 μm	5.01	2.68
10 μm	26.02	13.14

Table S2. The average spacing between pillars and the corresponding standard deviation measured by the SEM analysis. The average spacing is roughly 2.5x greater than the pillar diameter.

Mechanics Modelling Details:

A 2-D finite element model was developed in ABAQUS to qualitatively analyze the mechanical deformation of the 3-D current collector and polymer separator inside of a compressed coin cell. Details of the model's boundary conditions and loading are shown in Figure S20. The top of the separator is constrained from moving along the x-axis, while the base of the current collector is fully fixed to allow the separator to compress against it. A uniform pressure of 6.89 MPa (1000 PSI) is applied to the top of the separator. It should be noted that this model only considers linear elasticity, which may not be a valid assumption since stress concentrators will induce plasticity near the points of contact. Nevertheless, this model is intended to demonstrate a qualitative behavior in that the Cu pillars will remain undeformed under compression but the polymer separator will not. The material parameters needed for the model are shown in Table S2. The results of the model are shown in Figure S21. It is evident the separator does deform substantially and sink into the void space between the Cu pillars.

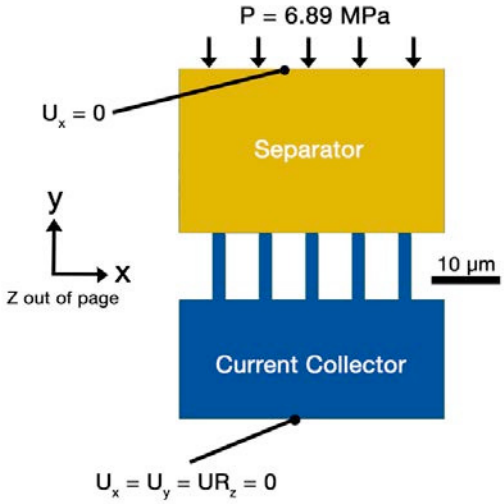

Figure S20. Geometry used in the ABAQUS model with boundary conditions shown.

	Young's modulus	Poisson's ratio	density [g cm^{-3}]
Polymer separator	200 MPa[14]	0.33[14]	1 (saturated with electrolyte)
Cu pillar	130 GPa	0.33	8.96

Table S3. Material parameters used in the ABAQUS model.

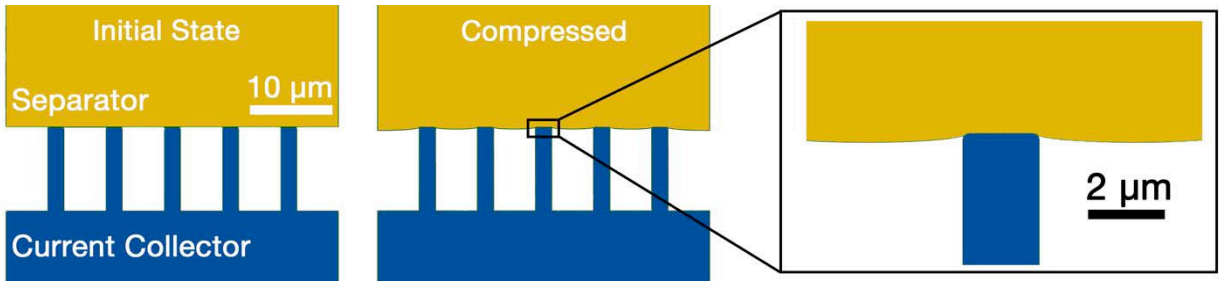

Figure S21. ABAQUS model results showing the deformation of the polymer separator.

Current Density Effect on Li Nucleation:

To demonstrate the impact of current density on nucleation, 0.5 mAh/cm^2 of Li was deposited onto planar Cu under various current densities of 1 mA/cm^2, 0.2 mA/cm^2, 0.1 mA/cm^2, and 0.05 mA/cm^2. As shown in Figure S22, lower nucleation densities and larger Li deposits were observed under reduced current densities.

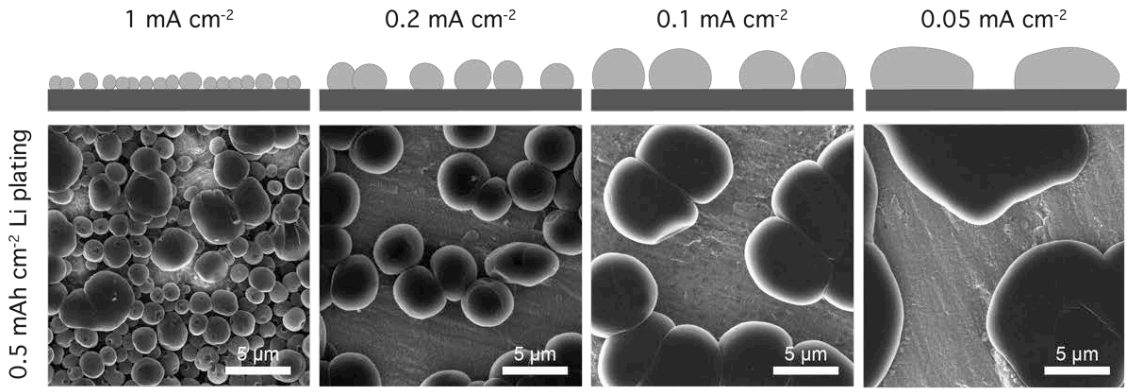

Figure S22. Schematics and SEM images of 0.5 mAh/cm^2 Li deposition on the planar Cu current collector under various current densities of 1 mA/cm^2, 0.2 mA/cm^2, 0.1 mA/cm^2, and 0.05 mA/cm^2.

If we assume a hypothetical situation, wherein current is perfectly uniform along the 0.2 µm Cu pillar arrays under a nominal current density of 1 mA/cm^2 (corresponding to a local current density of 0.05 mA/cm^2 due to 20x surface area enhancement compared to planar Cu), low-density Li nucleation would occur uniformly along the entire surface. However, the pore spacing between the 0.2 µm pillar arrays is only 0.5 µm, which is well below the observed diameter of the unconstrained Li deposits that form on planar Cu at 0.05 mA/cm^2 (Figure S22). As a result, growth of nuclei confined between pillars becomes more constrained and less favorable than growth of Li nuclei on the top surface (Figure S23). Therefore, subsequent Li deposition will preferentially occur on top of the pillar arrays as Li growth proceeds

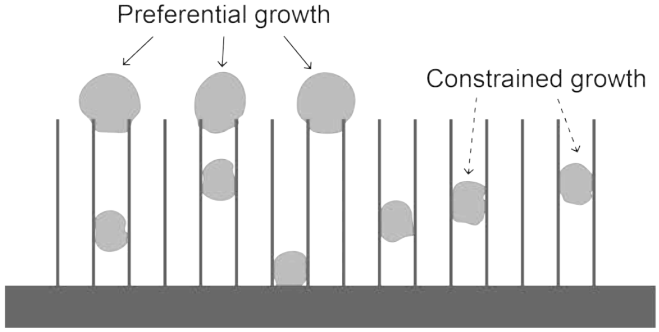

Figure S23. Schematic showing the constrained growth of Li nuclei confined between pillars and preferential growth of Li nuclei on the top surface of the 0.2 µm pillar arrays. Under the hypothetical scenario of uniform current density, the initial low-density nucleation occurs uniformly along the pillars. In reality, current focusing at the tips further promotes preferential nucleation on the top surface..

Experimental section:

1. Fabrication of vertically-aligned Cu pillar arrays

Cu pillar arrays were fabricated by templated electrodeposition on battery-grade Cu foils (18 μm thick, Oak Mitsui Inc.). The electrolyte bath consisted of 0.6 M $CuSO_4$ (Sigma-Aldrich) to provide Cu ions and 30 mM H_2SO_4 (Sigma-Aldrich) to increase solution conductivity (pH 1.8). A customized setup was designed where a polycarbonate track-etched (PCTE) membrane (47 mm diameter, Sterlitech Corp. and EMD Millipore) was sandwiched between two Cu foils. A piece of cellulose filter (Whatman) was immersed into the electroplating solution and then placed between the PCTE membrane and the counter Cu electrode to avoid short circuiting during electrodeposition. The setup was kept under a stack pressure by using clamps and was then connected to a potentiostat to perform Cu electrodeposition.

Electrodeposition of Cu was achieved using pulsed current technique to relax the concentration gradient within the small pores during the plating process. A repeated sequence of three steps was used: 1) A current pulse of 25 mA/cm^2 is applied to the cell for 50 ms; 2) A current pulse of 2 mA/cm^2 is applied to the cell for the next 250 ms; 3) The cell is rested for 600 ms. The pulse sequence was repeated until the targeted pillar length was reached.

After the electrodeposition, the sample was immersed into dichloromethane (Sigma-Aldrich) for 2 hr at 35 ^oC to dissolve the PCTE membrane, followed by O_2 plasma cleaning to remove organic residue and sulfuric acid etching to remove native oxides. Subsequently the sample was rinsed with deionized water and isopropyl alcohol, before being transferred into an argon-filled glovebox to prevent oxidation.

2. Atomic layer deposition of ZnO

Ultrathin ZnO films were deposited by atomic layer deposition (ALD) in a glovebox-integrated Savannah S200 (Veeco/Cambridge Nanotech Inc.). Diethylzinc and deionized water were used as the precursors with a pulse time of 1.0 s and 0.02 s, respectively. A carrier gas flow rate of 10 SCCM ultra-high purity Ar was used during purging. The purge time after each pulse was 30 s. The chamber temperature was kept at 150 ^oC throughout the deposition process. A lid-integrated in-situ quartz crystal microbalance was used to monitor film growth.

3. Coin cells assembly/testing

All air sensitive materials were handled in an argon-filled glovebox (MBRUAN) with oxygen and water levels < 1ppm. Li-Cu cells were assembled using CR-2032 coin cell cases, spacers, and wave springs (MTI Corp.). Celgard 2325 was used as the separator. 75 μL of electrolyte (Soulbrain) was used for each cell. The electrolyte was 1M LiTFSI in DOL:DME (1:1 volume ratio) with 1 wt% $LiNO_3$. Li metal foil (750 μm thick, Alfa Aesar) was used as the counter/reference electrode against the Cu working electrode, where both of them were punched into 1.6 cm^2 discs prior to cell assembly. A hydraulic crimping press (MTI Corp.) was used to compress coin cells to 1000 psi. The electrochemical performance of the coin cells was evaluated by galvanostatic charge/discharge on a Landt 2001a battery testing station.

4. Electrochemical measurements

Cyclic voltammetry experiments were scanned between a voltage range of 0-2 V (vs. Li/Li^+) at a scan rate of 0.5 mV/s on the Biologic VSP system. The electrolyte employed for the CV measurements was 1M LiTFSI in DOL:DME (1:1 volume ratio) with 1 wt% $LiNO_3$.

Three-electrode measurements were performed using a hermetically sealed glassware setup in the glovebox. The reference electrode was a scraped piece of Li metal foil. The data was collected using the bipotentiostat capabilities of the Biologic VSP system, which can measure the potential of the counter electrode and working electrode vs. reference electrode simultaneously. The cell assembled without presence of the polymer separator was also used the same setup.

5. Materials characterization

Cycled electrodes were collected from coin cells for SEM analysis. Cells were first uncrimped using a disassembly die in the same MTI crimping press and electrodes were removed and rinsed with fresh dimethyl carbonate for several times to remove electrolyte residue. The samples were then dried/stored in the glovebox antechamber. SEM images were obtained using Tescan MIRA3 FEG SEM and FEI Helios 650 Nanolab SEM.

TEM images were captured using JEOL 3011 HREM. The TEM sample was prepared by touching the lacey carbon TEM grid against the scraped Cu pillar array sample to pick up the Cu pillar.

A Kratos Axis Ultra was used for XPS analysis. A monochromated Al source was used with 160 eV pass energy and 700 x 300 μm sample area. An Ar ion source with 4kV accelerating voltage and 200 μA extractor current was used for sputtering off any surface film. CasaXPS was used for peak fitting with Shirley backgrounds.

6. Li wettability measurements

Sessile drop tests were performed to measure the contact angle of molten Li on pristine and ALD coated Cu substrates. Molten Li droplets were placed onto heated substrates from a heated syringe. Both the substrate surface and the syringe were kept at 200 ^oC. Importantly, the native layers present on the surface of the Li were removed from the molten Li source to achieve the deposition of purified molten Li onto the substrate surface. All experiments were performed inside an argon-filled glovebox, and high-resolution cross-sectional images were captured and digitally analyzed to determine contact angles.

Reference:

[1] S. Chen, J. Zheng, D. Mei, K. S. Han, M. H. Engelhard, W. Zhao, W. Xu, J. Liu, J. G. Zhang, *Adv. Mater.* **2018**, *1706102*, 1.

[2] Y. Liu, Y. K. Tzeng, D. Lin, A. Pei, H. Lu, N. A. Melosh, Z. X. Shen, S. Chu, Y. Cui, *Joule* **2018**, 1.

[3] L. Chen, K.-S. Chen, X. Chen, G. Ramirez, Z. Huang, N. R. Geise, H.-G. Steinrück, B. L. Fisher, R. Shahbazian-Yassar, M. F. Toney, M. C. Hersam, J. W. Elam, *ACS Appl. Mater. Interfaces* **2018**, *10*, 26972.

[4] S.-H. Wang, Y.-X. Yin, T.-T. Zuo, W. Dong, J.-Y. Li, J.-L. Shi, C.-H. Zhang, N.-W. Li, C.-J. Li, Y.-G. Guo, *Adv. Mater.* **2017**, *1703729*, 1703729.

[5] S. Liu, X. Xia, Y. Zhong, S. Deng, Z. Yao, L. Zhang, X.-B. Cheng, X. Wang, Q. Zhang, J. Tu, *Adv. Energy Mater.* **2017**, *1702322*, 1702322.

[6] C. Yang, Y. Yao, S. He, H. Xie, E. Hitz, L. Hu, *Adv. Mater.* **2017**, *29*, 1.

[7] Y. Liu, D. Lin, P. Y. Yuen, K. Liu, J. Xie, R. H. Dauskardt, Y. Cui, *Adv. Mater.* **2017**, *29*, 1.

[8] J. Lang, J. Song, L. Qi, Y. Luo, X. Luo, H. Wu, *ACS Appl. Mater. Interfaces* **2017**, *9*, 10360.

[9] L.-L. Lu, J. Ge, J.-N. Yang, S.-M. Chen, H.-B. Yao, F. Zhou, S.-H. Yu, *Nano Lett.* **2016**, *16*, 4431.

[10] W. Liu, D. Lin, A. Pei, Y. Cui, *J. Am. Chem. Soc.* **2016**, *138*, 15443.

[11] Q. Yun, Y.-B. He, W. Lv, Y. Zhao, B. Li, F. Kang, Q.-H. Yang, *Adv. Mater.* **2016**, *28*, 6932.

[12] C.-P. Yang, Y.-X. Yin, S.-F. Zhang, N.-W. Li, Y.-G. Guo, *Nat. Commun.* **2015**, *6*, 8058.

[13] B. D. Adams, J. Zheng, X. Ren, W. Xu, J.-G. Zhang, *Adv. Energy Mater.* **2017**, *1702097*, 1702097.

[14] C. Monroe, J. Newman, *J. Electrochem. Soc.* **2005**, *152*, A396.